Engineering 23 (2023) 73–81

Contents lists available at ScienceDirect

Engineering

journal homepage: www.elsevier.com/locate/eng

Research
Materials for Molecular Separations—Article

Membrane Contact Demulsification: A Superhydrophobic ZIF-8@rGO Membrane for Water-in-Oil Emulsion Separation

Jiahui Gu [a], Zhou Qu [a], Xiangning Zhang [d], Hongwei Fan [a,*], Chunxi Li [a], Jürgen Caro [c], Hong Meng [a,b,*]

[a] State Key Laboratory of Chemical Resource Engineering, College of Chemical Engineering, Beijing University of Chemical Technology, Beijing 100029, China
[b] State Key Laboratory of Chemistry and Utilization of Carbon-Based Energy Resources, College of Chemistry, Xinjiang University, Urumqi 830046, China
[c] Institute of Physical Chemistry and Electrochemistry, Leibniz Universität Hannover, Hannover D-30167, Germany
[d] Guangdong Engineering Technology Research Center of Advanced Insulating Coating, School of Chemistry and Chemical Engineering, South China University of Technology, Guangzhou 510640, China

ARTICLE INFO

Article history:
Received 15 October 2021
Revised 8 December 2021
Accepted 14 February 2022
Available online 21 February 2023

Keywords:
Water-in-oil emulsion
Demulsification
Oil/water separation
Superhydrophobic membrane

ABSTRACT

Achieving a water–oil interface imbalance has been identified as a critical factor in the demulsification of water-in-oil emulsions. However, conventional demulsifying membranes generally break the interface balance by depending on a relatively high transmembrane pressure. Here, we present a "contact demulsification" concept to naturally and quickly achieve disruption of the water–oil interface balance. For this purpose, a novel demulsifying membrane with a high flux of the organic component has been developed via the simple vacuum assembly of zeolitic imidazolate framework-8 (ZIF-8)@reduced graphene oxide (rGO) microspheres (ZGS) on a polytetrafluoroethylene (PTFE) support, followed by immobilization processing in a polydimethylsiloxane (PDMS) crosslinking solution. Due to the micro-nano hierarchies of the ZGS, the prepared ZIF-8@rGO@PDMS/PTFE (ZGPP) membranes feature a unique superhydrophobic surface, which results in a water–oil interface imbalance when a surfactant-stabilized water-in-oil emulsion comes into contact with the membrane surface. Under a low transmembrane pressure of 0.15 bar (15 kPa), such membranes show an excellent separation efficiency (~99.57%) and a high flux of 2254 $L \cdot m^{-2} \cdot h^{-1}$, even for surfactant-stabilized nanoscale water-in-toluene emulsions (with an average droplet size of 57 nm). This "contact demulsification" concept paves the way for developing next-generation demulsifying membranes for water-in-oil emulsion separation.

1. Introduction

Oil–water emulsions formed from industrial processes, daily life activities, and oilfield exploitation have resulted in severe environmental pollution and the waste of resources. Moreover, tiny amounts of water in fuel can condense on the metal surfaces of an engine, corroding the machine and shortening its service lifetime [1,2]. Therefore, the separation of water-in-oil emulsions is a crucial issue. The emulsified water droplets in oil–water emulsions are usually less than 20 μm in diameter and are incredibly stable due to surfactant adsorption at the oil/water interface [3–5]. Traditional separation methods such as gravity separation, skimming, gas flotation, or centrifugation can separate free-floating oil on water and immiscible oil–water mixtures but are not as effective for separating surfactant-stabilized water-in-oil emulsions (SSEs) [6–8].

Membrane technologies for oil–water emulsion separation are promising compared with traditional methods due to their low cost, low energy requirement, high separation efficiency, simple operation, and tunable pore size [9–11]. Although various kinds of hydrophobic/oleophilic membranes are frequently used in practical applications, they still have a main limitation [12]: They absorb both oil and water during separation, thus showing low selectivity and efficiency for emulsions. Moreover, the demulsification strongly depends on a relatively high transmembrane pressure (usually > 0.5 bar, 1 bar = 10^5 Pa) [13]. Consequently, the development of advanced membrane materials with the ability to selectively separate oil (or water) while completely repelling water (or oil) is highly desired for oil–water emulsion separation [14]. Super-wettable materials with totally different affinities toward

* Corresponding authors.
E-mail addresses: fanhongwei@mail.buct.edu.cn (H. Fan), menghong@mail.buct.edu.cn (H. Meng).

https://doi.org/10.1016/j.eng.2022.02.017

oils or water, which can break the water–oil interface balance due to strong interfacial effects, are promising for efficient oil–water emulsion separation [15]. Water-blocking materials, such as superhydrophobic/superoleophilic materials, have been used for water-in-oil emulsions [16–18]. Recently, superhydrophobic membranes, including nanofiber membranes [19,20], poly(vinylidene fluoride-*co*-hexafluoro-propylene) (PVDF–HFP)/polytetrafluoroethylene (PTFE) blend membranes [21], poly(vinylidene fluoride) (PVDF)-based membranes [22,23], poly(ether sulfone) (PES)-based membranes [24], polyphenylene sulfide (PPS)-based membranes [25], polysulfone (PSf)-based membranes [26], and other superhydrophobic membranes [27–29], have been studied and shown to effectively separate water-in-oil emulsions based on the "size-sieving" effect [30,31]. Constructing a superhydrophobic surface with a special structure is critical for water-in-oil emulsion separation.

Many superhydrophobic surfaces exist in nature, with the lotus leaf being a notable example. Unlike the Wenzel theory, which only discusses wetting behavior on a single scale, the lotus effect—which is also known as the multiscale effect—is mainly caused by the combination of a micro-nano hierarchical structure and low surface energy [32,33]. Inspired by the lotus effect, a variety of materials have been investigated in attempts to engineer superhydrophobic surfaces for water-in-oil emulsion separation [34–36]. In our previous work [37], we prepared a hybrid superhydrophobic/superoleophilic material consisting of a three-dimensional (3D) metal–organic framework (MOF)@reduced graphene oxide (rGO) microspheres with a unique micro-nano hierarchical structure. Wrinkled rGO nanosheets form a microscale 3D structure that ensures oil transfer, thereby improving the permeation performance of the organic component. As the nanoscale structure of MOF@rGO microspheres, hydrophobic zeolitic imidazolate framework-8 (ZIF-8) nanocrystals can effectively solve the problems of the agglomeration and stacking of graphene oxide (GO) nanosheets. The MOF@rGO microspheres have exhibited excellent performance in oil absorption, providing an alternative candidate for a robust superhydrophobic membrane for efficient oil–water emulsion separation.

Based on the above analysis, a novel superhydrophobic membrane was prepared in this study. As shown in Fig. 1, the ZIF-8@rGO microspheres (herein referred to as "ZGS") were deposited on PTFE supports by means of vacuum filtration. The 3D wrinkled ZGS were selected as a hybrid material due to their unique micro-nano hierarchical structures. The assembled ZGS on the PTFE substrate were immersed in a polydimethylsiloxane (PDMS) crosslinking solution to link the ZGS between themselves and to the PTFE support. Here, the composite ZGS@PDMS/PTFE is referred to as the "ZGPP membrane." Their combination of superwettability and abundant porosity indicates the potential of the resultant membranes for the efficient separation and demulsification of various SSEs. With high oil–water separation efficiency, such membranes are promising for practical oil purification and applications.

2. Results and discussion

2.1. Surface morphology analysis and wettability of ZGPP membranes

As shown in Fig. 1, the ZGPP membrane consists of three components: ZGS, PDMS, and PTFE. The interactions between the ZGS and PDMS, as well as those between the PDMS and PTFE, depend primarily on van der Waals forces. The crosslinked PDMS creates an intricate structure that traps the microspheres and fixes them tightly onto the PTFE substrate [38]. Due to the intertwining of the polymer chains, there is a strong adhesion between the PDMS and PTFE [39,40]. Fig. 2(a) shows scanning electron microscopy (SEM) image of the ZGS. The composite particles have a spherical shape with a diameter of 3–5 μm and a unique micro-nano hierarchical structure. The PTFE substrate is a commercial microfiltration membrane with a mean pore size of 0.22 μm (Fig. 2(b)). Membranes with ZGS loadings of 0, 0.15, 0.50, 1.00, 2.00, or 4.00 $mg \cdot cm^{-2}$ are referred to as ZGPP-0, -0.15, -0.5, -1, -2, or -4, respectively. PDMS segments with a low surface energy were used to immobilize the ZGS on the PTFE substrate. Compared with the original PTFE substrate, the pore size of the ZGPP-0 membrane is reduced (Fig. 2(c)) due to the presence of PDMS in the micropores of the PTFE substrate. Depending on the amount of deposited ZGS, the surface of the ZGPP membranes exhibits different morphologies. When the ZGS loading is low (i.e., 0.15–1.00 $mg \cdot cm^{-2}$), the ZGS cannot completely cover the membrane surface, leaving some blank areas (Fig. 2(d); Figs. S1 and S2(b)–(d) in Appendix A). However, for higher ZGS loadings (i.e., 2–4 $mg \cdot cm^{-2}$), the ZGS are uniformly dispersed and form a homogeneous multi-particle layer on the PTFE surface (Figs. 2(e) and (f)) with a thickness of 20–37 μm (Figs. S2(e) and (f) in Appendix A). Despite the PDMS treatment, the 37 μm ZGS top layer of the ZGPP-4 membrane was damaged during handling due to the weak interaction between the ZGS. Therefore, the ZGPP-2 membrane showed the best morphology (Fig. 2(e)), and this membrane was studied in detail.

The distribution of the different moieties on the membrane surface was confirmed by means of energy-dispersive X-ray spectroscopy (EDXS). As shown in Figs. 2(g)–(l), the elements carbon (C), oxygen (O), zinc (Zn), silicon (Si), and fluorine (F) can be detected on the surface of the ZGPP-2 membrane. The Zn (La1_2) originates from the ZIF-8 nanoparticles of the ZGS, as shown in Fig. 2(j). The homogeneous distribution of the Zn element indicates that the ZIF-8 nanoparticles are uniformly dispersed on the ZGS surface. The Si (Ka1) indicates that the PDMS uniformly covers the surface of the ZGPP-2 membrane without an obviously uneven distribution (Fig. 2(k)). The F (Ka1_2) originating from the PTFE substrate is rarely detected, indicating that the ZGS cover the surface of the PTFE substrate completely (Fig. 2(l)).

The surface composition of the ZGPP membranes was studied using X-ray photoelectron spectroscopy (XPS). The results from XPS, as shown in Fig. 2(m), indicate that the peaks of N 1s are located at the binding energy of 401.8 eV, which indicates the presence of ZIF-8 near to the surface of the ZGPP membranes.

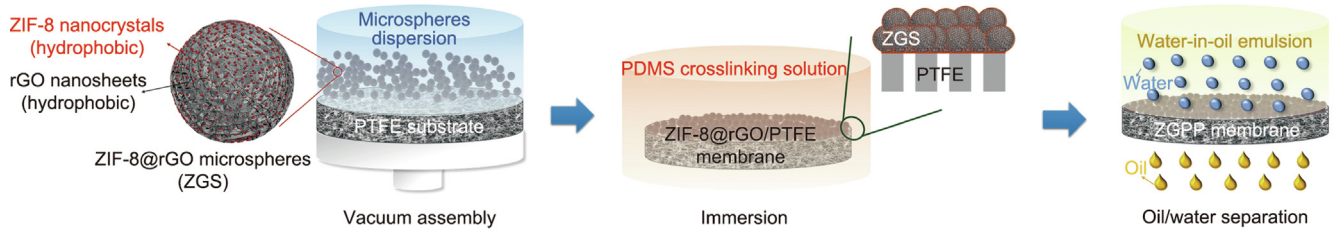

Fig. 1. Schematic of the preparation of the composite ZGS@PDMS/PTFE (ZGPP membrane) for the separation of an organic component from water-in-oil emulsions. PDMS: polydimethylsiloxane.

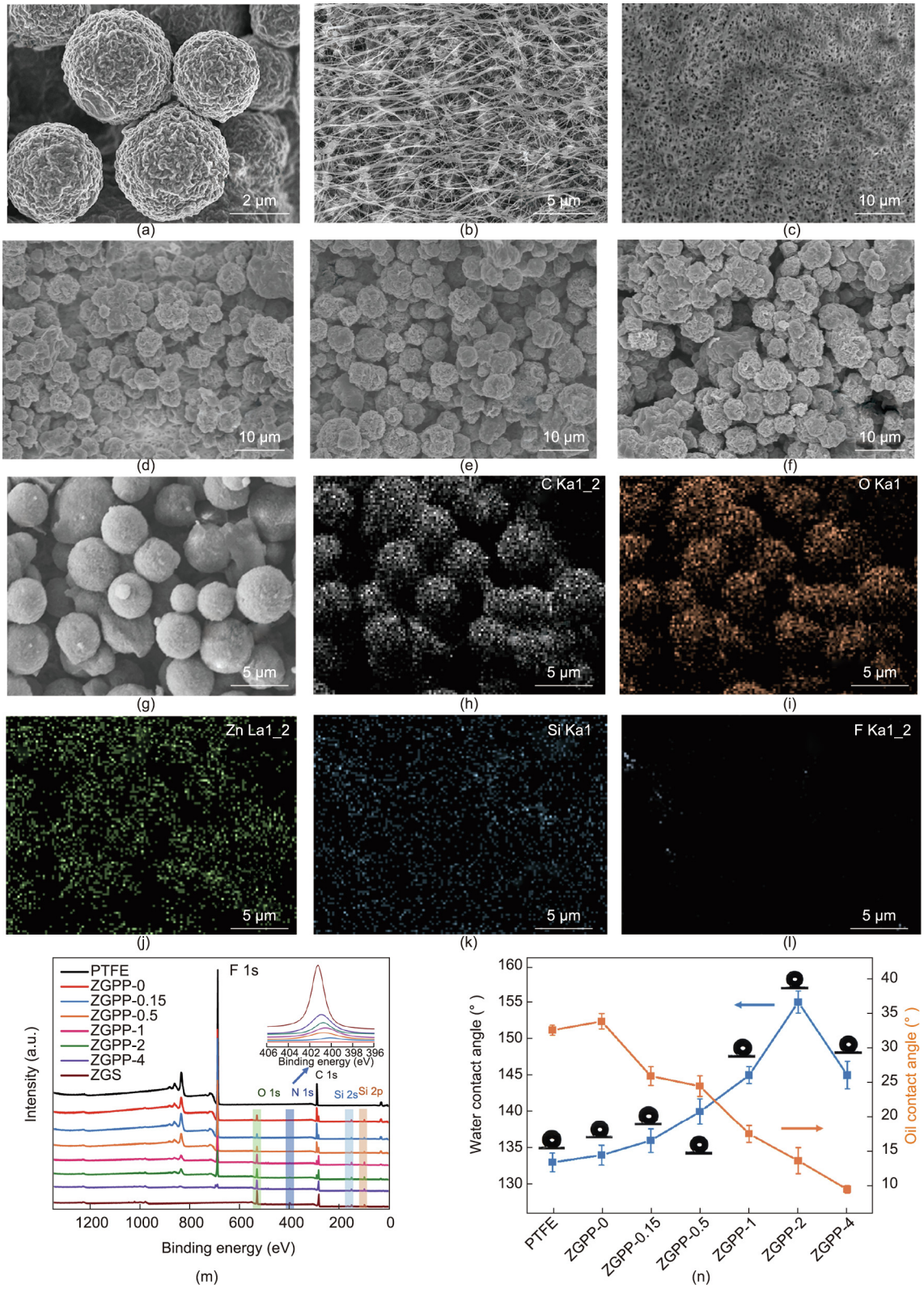

Fig. 2. (a–f) SEM images of (a) ZGS; (b) the PTFE commercial microfiltration membrane (mean pore size: 0.22 μm); and (c–f) ZGPP membranes with (c) ZGPP-0, (d) ZGPP-1, (e) ZGPP-2, and (f) ZGPP-4. (g–l) EDXS mapping images of the ZGPP-2 membrane. (m) XPS wide-scan results of the membranes. (n) Contact angles of water and oil (toluene) with the ZGPP membrane surface in air at room temperature.

The peaks of F 1s at about 689.8 eV (from the PTFE substrate) decrease with an increasing loading of ZGS. Two peaks of C 1s from the ZGPP membranes that correspond to the C–F bond at 292.08 eV and the C–Si bond at 285.08 eV gradually disappear with an increasing ZGS loading, indicating a good dispersion of the ZGS on the surface of the ZGPP membrane. Furthermore, according to the detection depth of 10 nm by XPS, the growing peaks of N 1s and O 1s demonstrate that the thickness of the PDMS layer is less than 10 nm. Similar information from the Fourier-transform infrared (FTIR) spectra is recorded in Fig. S3 in Appendix A, which

shows that the C–F bond stretching vibration peaks from the PTFE substrate are confirmed at 1215 and 1150 cm^{-1}. The Si–O bond stretching vibration peak, the C–Si bond stretching vibration peak, and the C–H bond stretching vibration peak from PDMS correspond to the peaks at 1018, 804, and 2965 cm^{-1}, respectively. This finding is in agreement with the results from XPS—namely, that the intensity of the C–F bond signal decreases gradually with an increasing ZGS loading, which verifies that the PTFE substrate is increasingly covered by ZGS.

In order to evaluate the surface wettability of the ZGPP membranes, contact angles were measured, as shown in Fig. 2(n). In complete accordance with our previous work [37], the ZGS show excellent superhydrophobicity, with a water contact angle (WCA) of 158° in air. With an increase in the ZGS loading, the WCA of the ZGPP membranes increases at first and then decreases. However, excess ZGS loading is prone to aggregation and stacking, causing a large surface height difference. In this case, the gaps between the ZGS are unevenly distributed, and the advantages of the micro-nano structure on the membrane surface cannot fully play out. Moreover, ZGS tend to peel off when the ZGS loading increases to 4 $mg{\cdot}cm^{-2}$, resulting in the destruction of the surface micro-nano hierarchical structure and a subsequent decrease in the WCA. A maximum WCA of 155° was found on the ZGPP-2 membrane, clearly indicating its superhydrophobicity.

For oil droplets in contact with the surface of the ZGPP membranes, the oil wettability was observed by means of oil contact angles (OCAs) in air and the contact time of the oil droplets. Due to the membranes' unique structure and the filler ZGS, the oleophilicity of the ZGPP membranes is enhanced, with a gradually decreasing OCA with increased ZGS loading. As shown in Fig. S4 in Appendix A, the pores of the superoleophilic ZGS and the free volume of PDMS between the ZGS of the membrane are transport-active to the permeation of the organic phase (e.g., toluene or ethanol) through the surface of the ZGPP membrane. The higher the ZGS loading of the ZGPP membrane, the shorter the contact time of the oil droplet with the surface of the ZGPP membrane before being absorbed by the membrane. The contact angle values indicate that the micro-nano hierarchical structure of the ZGS plays a dominant role in the superhydrophobicity of the ZGPP membranes.

2.2. SSEs separation performance of the ZGPP membranes

To evaluate the separation potential of the ZGPP membranes for water-in-oil emulsion, SSEs based on an organic solvent (toluene, petroleum ether, or *n*-heptane) with different water contents were prepared, and the average droplet size of the SSEs was measured by means of dynamic light scattering (DLS), as shown in Fig. S5 in Appendix A. The as-prepared superhydrophobic ZGPP membrane was stuck in the middle of a vacuum filter; then, the SSE was poured onto the membrane and quickly spontaneously permeated it. The emulsion based on toluene with an average droplet size of 240 nm, named SSE-240, was studied in detail. As shown in Fig. 3(a), SSE-240 was successfully separated with a high oil–water separation efficiency. As the ZGS loading increased, the separation efficiency of the ZGPP membranes obviously increased from 92.53% to 99.61%, and the flux slightly improved. The oil purity of the permeate was over 99.99%. In this work, ZGPP-2 can be regarded as the optimal membrane with the highest separation efficiency and an excellent permeate flux. Even when the transmembrane pressure was increased (0.15–0.50 bar), the separation efficiency for SSE-240 on the ZGPP-2 membrane was still over 98.2% (Fig. S6 in Appendix A). The increase from the hydrophobicity to the superhydrophobicity of the ZGPP membranes improved the separation efficiency for the SSEs.

Digital pictures of the SSE-240 before and after separation were taken (Fig. 3(b)). After separation by the ZGPP-2 membrane, the milky feeding emulsion turned into a transparent permeate, indicating the good separation performance of the membrane. Images of the feed (SSE-240) and the permeate taken by optical microscope are provided in Fig. 3(b) and show tiny water droplets nearly disappearing after separation. In addition, the droplet size distributions of the emulsion before and after separation were measured. As shown in Fig. 3(c), the size of the water droplets in the emulsion before separation had a wide distribution, ranging from 43 to 955 nm. Most of the droplets with a size of 200–850 nm disappeared in the permeate, which contained less than 0.01 wt% water. However, some droplets with a size of 4–7 nm were detected via DLS in the permeate (Fig. 3(d)); these are ascribed as being micelles formed by the dissolved surfactants and not water droplets [41]. After separation, the maximum of the size distribution of the water droplets in the retentate shifted to a higher value (Fig. 3(e)), which can be explained by the coalescence of the water droplets.

A variety of SSEs were prepared to further demonstrate the emulsion separation performance of the ZGPP membranes. Figs. 3(f) and (g) show the separation performance of the ZGPP-2 membrane for different SSEs. When a slight transmembrane pressure of 0.15 bar was applied, a high toluene flux of 2254 $L{\cdot}m^{-2}{\cdot}h^{-1}$ and an excellent separation efficiency for toluene/water of 99.57% were measured for SSE with an average droplet size of 57 nm (SSE-57). In comparison, traditional membranes usually require a higher transmembrane pressure to achieve efficient demulsification and separation (Table S2 in Appendix A). For example, in the case of a PTFE/fluorinated ethylene propylene (FEP) membrane, the toluene flux was only 134–204 $L{\cdot}m^{-2}{\cdot}h^{-1}$ under a transmembrane pressure of 0.5 bar [13].

According to the droplet size distributions, SSE-57 is a nano-emulsion, which can increase the contact area of the emulsified water droplets and the membrane surface. With an increase in the contact area, the balance of water and oil in the nano-emulsion is disturbed, increasing the separation performance. The emulsions changed from being milky in the feed to transparent in the permeate after passing through the ZGPP-2 membrane, indicating even by eyesight the high demulsification potential of the ZGPP membrane. Considering that the transmembrane pressure used in our work is 3–10 times lower than the reported pressure (Table S2), this excellent separation performance for both micro- and nano-emulsions indicates that the demulsification process in the ZGPP-2 membrane is mainly based on the contact demulsification mechanism.

To further demonstrate the contact demulsification process, experiments were done on a series of SSEs without transmembrane pressure. As shown in Fig. 3(h), the ZGPP-2 membrane could demulsify SSEs with different average droplet sizes. When tested as a control experiment, an oleophilic PTFE substrate could not demulsify the SSEs. For a range of average droplet sizes from 126 to 1161 nm, the ZGPP-2 membrane could demulsify a water-in-oil emulsion within 53–200 min. As shown in Fig. S7 in Appendix A, progressive demulsification begins at 20 min into the separation; this is followed by the enlargement of the clarified area, which takes 70 min, until the milky emulsion becomes entirely transparent, indicating that the water-in-oil emulsion SSE-240 is successfully demulsified. The water content in the supernatant was unmeasurable low (< 0.01 $\mu g{\cdot}\mu L^{-1}$), as evaluated with a Karl Fischer analyser. Even for nano-emulsions with droplet sizes < 100 nm, the ZGPP-2 membrane showed a good demulsifying capacity. For example, in the case of an average droplet size of 57 nm (SSE-57), after remaining at room temperature for 200 min, the SSE-57 changed to half oil and half emulsion using the ZGPP-2 membrane (Fig. S8 in Appendix A). When the temperature was increased to 40 °C, the nano-emulsion was demulsified entirely after 180 min (Fig. S9 in Appendix A).

The contact demulsification process was further confirmed using ultraviolet visible (UV–vis) absorbance at wavelength of

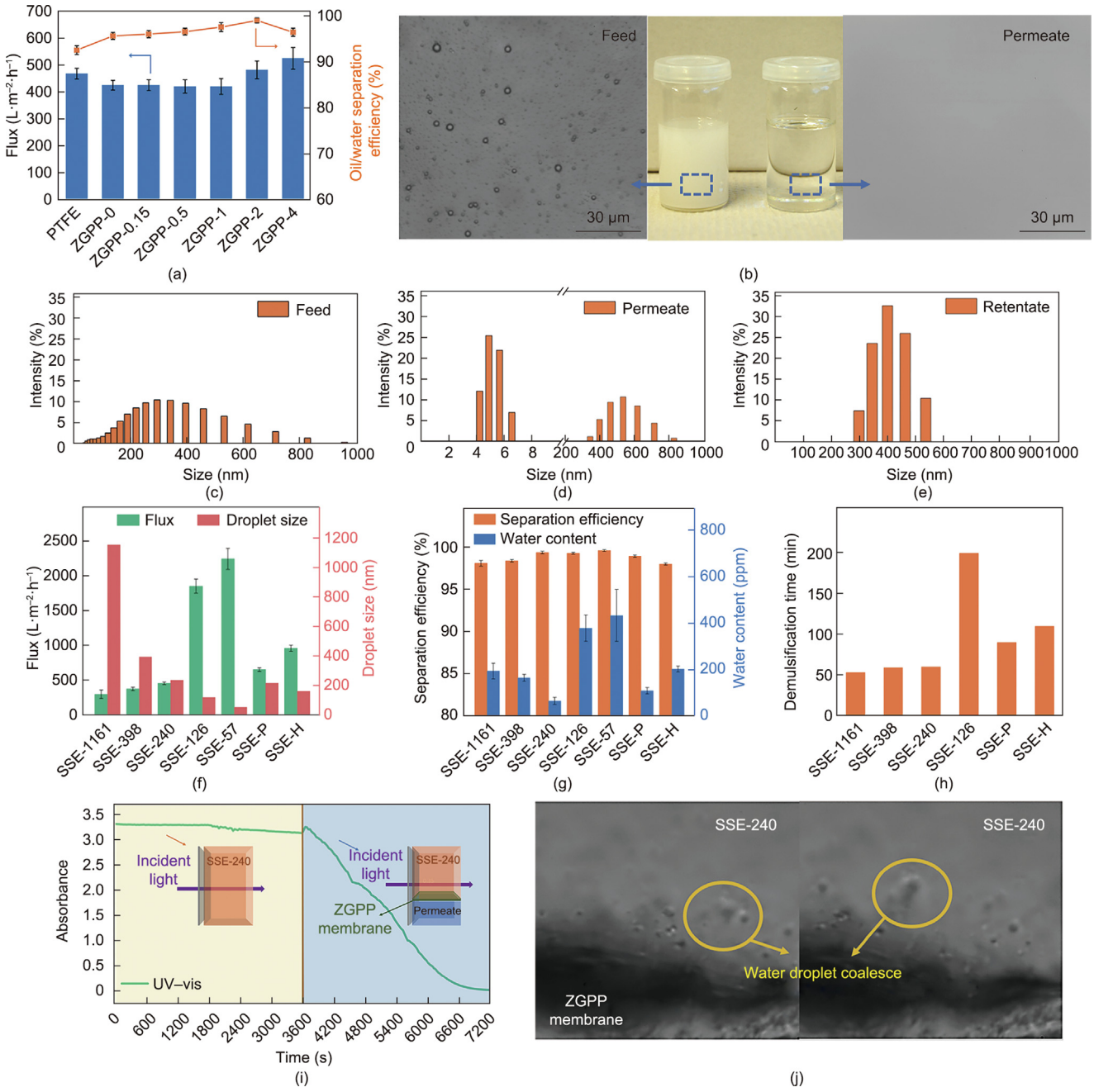

Fig. 3. (a) Oil–water separation of SSE-240 on the ZGPP membranes at room temperature when applying a slight transmembrane pressure of 0.15 bar. (b) Optical microscopy images and a digital photo of the feed and permeate separation (SSE-240) by the ZGPP-2 membrane. (c–e) Droplet size distributions of the SSE-240 in the feed, permeate, and retentate separated by the ZGPP-2 membrane. (f) Separation flux and average droplet size of SSEs on the ZGPP-2 membrane (room temperature, 0.15 bar). (g) Separation efficiency and water content of the permeate on the ZGPP-2 membrane for different SSEs (room temperature, 0.15 bar). (h) Demulsification time of the ZGPP-2 membrane for a series of SSEs (room temperature, without transmembrane pressure). (i) UV–vis absorbance of the SSE-240 emulsion with and without the ZGPP-2 membrane during demulsification (wavelength: 500 nm). (j) Optical microscopy images of water droplets coalescing during demulsification. The video (Movie S1) is provided in Appendix A. SSE-1161, SSE-398, SSE-126, and SSE-57 stand for SSE based on toluene with an average droplet size of 1161, 398, 126, and 57 nm, respectively. SSE-P and SSE-H stand for SSE based on petroleum ether and *n*-heptane, respectively. Details shown in Table S1.

500 nm for 2 h, as shown in Fig. 3(i). Taking the SSE-240 emulsion as an example, the original SSE-240 had a high and stable absorbance (~3.25) in the range of 0–3600 s. This high absorbance means a low transmittance, due to the presence of SSE-240 emulsion droplets. The stable absorbance value indicates the excellent stability and uniformity of the emulsion solution. After placing a ZGPP-2 membrane in the cuvette, the absorbance of the solution decreased significantly as the standing time increased. When the standing time was 7200 s, the absorbance was close to 0. This observation suggests that the SSE-240 emulsion droplets tend to coalesce in the presence of the ZGPP-2 membrane (Fig. 3(j)), destroying the stability of the emulsion solution and thus leading to the demulsification of SSE-240.

2.3. Mechanism analysis of separation

To further reveal the underlying mechanism of the separation, the proton transverse relaxation time T_2 was measured by means of low-field nuclear magnetic resonance (LF-NMR) to analyze information regarding the void size or degree of molecular confinement

within the membranes. A T_2 distribution corresponds to a pore size distribution, with molecules in the smallest pores having the shortest relaxation times and molecules in the largest pores having the longest relaxation times [42]. A T_2 signal that is less than 100 was normally ascribed to the binding of toluene at the surface. For the PTFE support filled with toluene, two T_2 signals were observed (Fig. S10 in Appendix A) at 10^2–10^3 and 10^3–10^4 ms, which were ascribed to toluene in the pores of the membrane for pore sizes of less than 100 nm and larger than 100 nm, respectively. Interestingly, after preparing the ZGPP membrane, the T_2 signal at 10^2–10^3 ms disappeared because the PTFE pores were filled with PDMS. The pores of the ZIF-8 nanocrystals have been crystallographically measured to be 0.34 nm normally, but given the framework flexibility, it could stretch to about 0.43 nm wide. This size does not allow the adsorption and diffusion of toluene through the pores (as the critical molecule size of toluene is 0.59 nm). Therefore, the toluene in the ZGS only shows a T_2 signal at 10^3–10^4 ms. With an increase in the ZGS loading, the areas of the T_2 signals of the ZGPP membranes between 10^3 and 10^4 ms tended to decrease, and the T_2 relaxation times of these signals gradually approached those of the ZGS.

When a droplet remains stably on an ideal surface, thermodynamic equilibrium is achieved among the gas/liquid/solid three-phase interface, as shown in Fig. S11 in Appendix A and described by Young's equation:

$$\cos\theta = \frac{\gamma_{s\text{-}g} - \gamma_{l\text{-}s}}{\gamma_{l\text{-}g}} \quad (1)$$

where θ is the contact angle, $\gamma_{s\text{-}g}$ is the surface tension at the solid/gas interface, $\gamma_{l\text{-}g}$ is the surface tension at the liquid/gas interface, and $\gamma_{l\text{-}s}$ is the surface tension at the liquid/solid interface.

It is well known that liquids with a $\gamma_{l\text{-}g}$ less than the critical surface tension can spread on the surface of the solid. Therefore, to further analyze the interfacial effects of toluene molecules on the membrane surface, the critical surface tensions of various membranes were calculated by means of the Zisman plot method using a contact angle analyzer. When the critical surface tension of the membrane is close to the surface tension of the liquid in air, the liquid spreads more easily on the surface of the membrane. As shown in Fig. S12 in Appendix A, the critical surface tension of the PTFE substrate is 15.3 $mN{\cdot}m^{-1}$. The critical surface tensions of the ZGPP membranes gradually increase with an increase in the ZGS loading. In the case of the ZGPP-4 membrane, the critical surface tension reaches 23.16 $mN{\cdot}m^{-1}$, which is near to the $\gamma_{l\text{-}g}$ of toluene, at 28.83 $mN{\cdot}m^{-1}$ (in air, 293 K). This suggests that the oleophilicity of the membrane surface greatly improved with an increase in the ZGS loading.

The ZGPP-2 membrane shows an underoil (petroleum ether) WCA of 145.0° ± 0.9° (Fig. S13 in Appendix A). When a water droplet stays on a solid surface in oil, there is thermodynamic equilibrium among the oil/water/solid three-phase interface, according to Young's equation. Therefore, the surface tension of the solid/oil interface must be less than the surface tension of the water/solid interface when the surface of the solid is hydrophobic, which means that the surface of the ZGPP membrane has a stronger affinity to oil than to water. The surface tension of the water/oil interface is unstable if the oil around the water droplets is absorbed by the membrane, causing the emulsified droplets to be broken easily and allowing the water to coalesce.

2.4. Molecular dynamics simulation analysis

To further understand the mechanism of the contact demulsification, molecular dynamics (MD) simulations were performed for the interaction of surfactant-stabilized water-in-oil (toluene) emulsions with ZGS surfaces and an rGO surface (Fig. S14 in Appendix A). Fig. 4(a) shows snapshots taken during the simulation demulsification process of a surfactant-stabilized water-in-toluene emulsion at the bent surface of the ZGS. The water droplets can coalesce, thus demulsifying and separating the water-in-oil emulsion. The simulation shows the coalescence of four water–span 80 (surfactant) nano-droplets at 0.4, 0.7, and 8.3 ns. Then four water–span 80 (surfactant) nano-droplets fully coalesce at 8.6 ns and remain coalesced at 30 ns. Fig. 4(b) shows snapshots of the surfactant-stabilized water-in-toluene emulsion at the bent surface of the rGO nanosheet. The four water–span 80 nano-droplets did not finish coalescing during the simulation time.

For a quantitative analysis of the contact demulsification process, the interaction energies were calculated. As shown in Fig. 4(c), all energies of interaction with ZGS or rGO are negative, indicating that the force is attractive. With the hydrophobic ZIF-8 nanocrystal, the ZGS show significantly less interaction energy (-10.7 $kJ{\cdot}mol^{-1}$) to water compared with the interaction energy between the rGO nanosheets and water (-62.2 $kJ{\cdot}mol^{-1}$). Compared with the interaction energy to toluene from the rGO nanosheets ($-69\,794.4$ $kJ{\cdot}mol^{-1}$), the interaction energy to toluene from the ZGS seems to increase to $-82\,784.8$ $kJ{\cdot}mol^{-1}$. All these changes indicate that the unique micro-nano hierarchical structure of the ZGS, including the ZIF-8 nanocrystal and the wrinkled rGO nanosheets, efficiently enhance the hydrophobicity and oleophilicity of the membrane.

For a further analysis of the interaction energies, the Coulomb energy (E_{coul}) and van der Waals energy (E_{vdw}) were respectively calculated. As shown in Fig. 4(d) for the ZGS–water, ZGS–span 80, and ZGS–toluene, the Coulomb energy is far less than the van der Waals energy, suggesting that the van der Waals forces are the dominant force between the ZGS and the emulsions. Since the van der Waals energy and Coulomb energy for ZGS–water are much lower than those of the ZGS–span 80 and ZGS–toluene, the attractive force between the ZGS and water is much weaker due to the superhydrophobicity of the ZGPP membrane (Fig. 2(n)). Therefore, when the water-in-oil (toluene) emulsion moves to the surface of the ZGPP membrane, the strong attractive force between the ZGS and span 80 or toluene can initially break the interface balance of the span 80 and water droplets, causing the water nano-droplets to move and coalesce (Fig. 3(j); Movie S1 in Appendix A). Subsequently, the toluene can easily permeate through the membrane because of the high van der Waals forces between the ZGS and toluene (Fig. S15 in Appendix A). In this study, the formation of enlarged water droplets in the retentate was also studied using DLS. As shown in Fig. 3(e), the maximum water droplet size distribution of the retentate increases to 408 nm, which further confirms the coalescence of the rejected water nano-droplets during the contact demulsification process.

Fig. 4(e) shows the minimum distance between the ZGS or rGO and water during the simulation. As a comparison, the minimum distance of rGO–water is about 0.16 nm at 5.5 ns; then, the minimum distance is maintained until the end of the simulation, which suggests the absorption of water on the rGO nanosheets. The minimum distance of ZGS–water fluctuates greatly during the whole simulation time, indicating that it is difficult for the water to be adsorbed by ZGS and that it will not pollute the membrane. The minimum distance between the ZGS or rGO and span 80 shows the same results during the simulation (Fig. 4(f)). The fluctuating minimum distance between ZGS–span 80 and ZGS–water indicates the easy cleaning of the ZGPP membranes.

Furthermore, to evaluate the stability of the ZGPP-2 membrane, cyclic SSE-240 separation experiments were conducted, as shown in Fig. 5(a). No obvious deterioration in the separation performance was observed after 100 min, while the separation efficiency was 99.2% and the flux was 730 $L{\cdot}m^{-2}{\cdot}h^{-1}$. Due to the limitation of the dead-end filtration method, membrane pollution occurred in the separation process. However, the ZGPP membranes show an

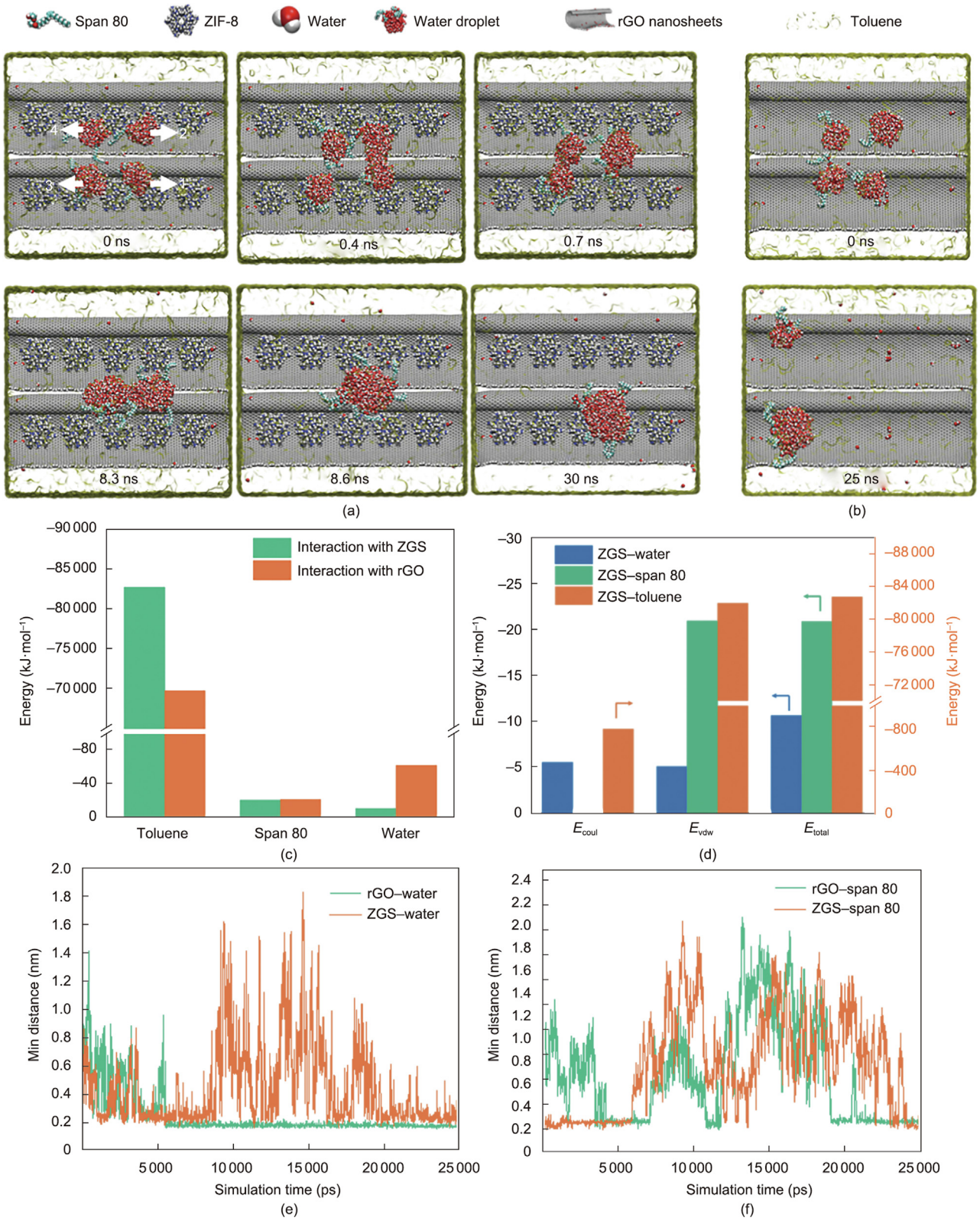

Fig. 4. (a) Snapshots of the demulsification process of the surfactant-stabilized water-in-toluene emulsion on the surface of ZIF-8@rGO nanosheets; the toluene inside is showed as a glass bubble for clarity. (b) Snapshots of the MD simulation process of the surfactant-stabilized water-in-toluene emulsion on the surface of rGO nanosheets. (c) Interaction energies between ZGS or rGO and water/span 80/toluene during the simulation time. (d) Energy between the ZGS and water, span 80, and toluene during the simulation demulsification. (e) Minimum (Min) distance between the ZGS or rGO and water during the simulation time. (f) Minimum distance between the ZGS or rGO and span 80 during the simulation time.

anti-fouling ability, and their separation performance can be restored by simple washing. It was also noted that, after 8 cycles of use, a very small number of free ZGS might be peeled off, which slightly increases the separation flux. Nevertheless, as is clearly shown in Fig. 5(b), after ten separation cycles, the ZGPP-2 membrane still shows a high WCA and a good distribution of the ZGS

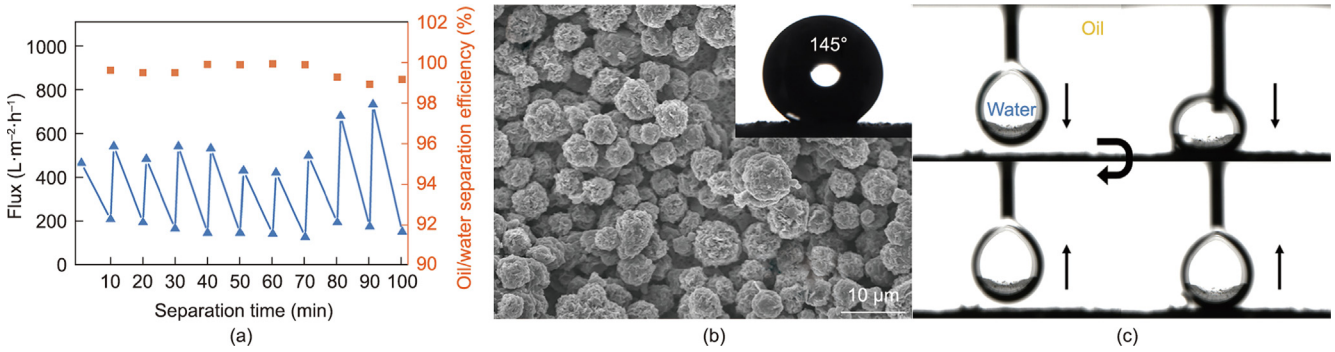

Fig. 5. (a) Stability of the ZGPP-2 membrane. (b) SEM image of the ZGPP-2 membrane after ten cycles, with a WCA in air of 145° shown in the insert image. (c) The approaching, contacting, and detaching process between a water droplet in oil (petroleum ether) and the ZGPP-2 membrane.

on its surface. Fig. 5(c) shows the approaching, contacting, and detaching process between a water droplet in oil (petroleum ether) and the ZGPP-2 membrane. The water droplet can easily bounce off the surface of the ZGPP-2 membrane, even under severe deformation. These results are indicative of the excellent durability and stability of the ZGPP-2 membrane, suggesting that the ZGPP membranes are promising for water-in-oil emulsions separation.

3. Conclusions

In summary, a "contact demulsification" concept was proposed to design an advanced demulsifying membrane for water-in-oil emulsion separation. The novel demulsifying membrane was achieved by means of a vacuum assembly of ZGS on a PTFE support, followed by crosslinking with PDMS. Manipulation of the ZGS loading enabled the creation of a membrane with superhydrophobic and enhanced oleophilic surface properties, which can achieve natural and rapid demulsification. These membranes show excellent emulsion separation efficiency and high fluxes of the organic component for both microscale and nanoscale SSEs. We believe that membrane contact demulsification holds great potential for the efficient separation of surfactant-stabilized emulsions.

Acknowledgments

This work was financially supported by the National Natural Science Foundation of China (51773012), Fundamental Research Funds for the Central Universities (buctrc202135), and China Scholarship Council Program (201906880031).

Compliance with ethics guidelines

Jiahui Gu, Zhou Qu, Xiangning Zhang, Hongwei Fan, Chunxi Li, Jürgen Caro, and Hong Meng declare that they have no conflict of interest or financial conflicts to disclose.

Appendix A. Supplementary data

Supplementary data to this article can be found online at https://doi.org/10.1016/j.eng.2022.02.017.

References

[1] Ghaffar A, Chen C, Zhu X, Chen B. Underwater superoleophobic PVA–GO nanofibrous membranes for emulsified oily water purification. Environ Ence Nano 2019;6(12):3723–33.
[2] Zeng X, Qian L, Yuan X, Zhou C, Li Z, Cheng J, et al. Inspired by *Stenocara* beetles: from water collection to high-efficiency water-in-oil emulsion separation. ACS Nano 2017;11(1):760–9.
[3] Zhang W, Liu N, Cao Y, Lin X, Liu Y, Feng L. Superwetting porous materials for wastewater treatment: from immiscible oil/water mixture to emulsion separation. Adv Mater Interfaces 2017;4(10):1600029.
[4] Chen C, Chen S, Chen L, Yu Y, Weng D, Mahmood A, et al. Underoil superhydrophilic metal felt fabricated by modifying ultrathin fumed silica coatings for the separation of water-in-oil emulsions. ACS Appl Mater Interfaces 2020;12(24):27663–71.
[5] Wei Y, Qi H, Gong X, Zhao S. Specially wettable membranes for oil–water separation. Adv Mater Interfaces 2018;5(23):1800576.
[6] Cheryan M, Rajagopalan N. Membrane processing of oily streams. Wastewater treatment and waste reduction. J Membr Sci 1998;151(1):13–28.
[7] Tummons E, Han Q, Tanudjaja HJ, Hejase CA, Chew JW, Tarabara VV. Membrane fouling by emulsified oil: a review. Sep Purif Technol 2020;248:116919.
[8] Zhang W, Shi Z, Zhang F, Liu X, Jin J, Jiang L. Superhydrophobic and superoleophilic PVDF membranes for effective separation of water-in-oil emulsions with high flux. Adv Mater 2013;25(14):2071–6.
[9] Macedonio F, Drioli E. Membrane engineering for green process engineering. Engineering 2017;3(3):290–8.
[10] Zhang G, Jin W, Xu N. Design and fabrication of ceramic catalytic membrane reactors for green chemical engineering applications. Engineering 2018;4(6):848–60.
[11] Dai L, Huang K, Xia Y, Xu Z. Two-dimensional material separation membranes for renewable energy purification, storage, and conversion. Green Energy Environ 2021;6(2):193–211.
[12] Wang F, Lei S, Xue M, Ou J, Li W. *In situ* separation and collection of oil from water surface via a novel superoleophilic and superhydrophobic oil containment boom. Langmuir 2014;30(5):1281–9.
[13] Huang Y, Xiao C, Huang Q, Liu H, Guo Z, Sun K. Robust preparation of tubular PTFE/FEP ultrafine fibers-covered porous membrane by electrospinning for continuous highly effective oil/water separation. J Membr Sci 2018;568:87–96.
[14] Xue Z, Wang S, Lin L, Chen L, Liu M, Feng L, et al. A novel superhydrophilic and underwater superoleophobic hydrogel-coated mesh for oil/water separation. Adv Mater 2011;23(37):4270–3.
[15] Yong J, Huo J, Chen F, Yang Q, Hou X. Oil/water separation based on natural materials with super-wettability: recent advances. Phys Chem Chem Phys 2018;20(39):25140–63.
[16] Liu YQ, Zhang YL, Fu XY, Sun HB. Bioinspired underwater superoleophobic membrane based on a graphene oxide coated wire mesh for efficient oil/water separation. ACS Appl Mater Interfaces 2015;7(37):20930–6.
[17] Lin X, Heo J, Jeong H, Choi M, Chang M, Hong J. Robust superhydrophobic carbon nanofiber network inlay-gated mesh for water-in-oil emulsion separation with high flux. J Mater Chem A 2016;4(46):17970–80.
[18] Yin X, Wang Z, Shen Y, Mu P, Zhu G, Li J. Facile fabrication of superhydrophobic copper hydroxide coated mesh for effective separation of water-in-oil emulsions. Sep Purif Technol 2020;230:115856.
[19] Kang H, Zhang X, Li L, Zhao B, Ma F, Zhang J. Polydopamine and poly(dimethylsiloxane) modified superhydrophobic fiberglass membranes for efficient water-in-oil emulsions separation. J Colloid Interface Sci 2020;559:178–85.
[20] Huang M, Si Y, Tang X, Zhu Z, Ding B, Liu L, et al. Gravity driven separation of emulsified oil–water mixtures utilizing *in situ* polymerized superhydrophobic and superoleophilic nanofibrous membranes. J Mater Chem A 2013;1(45):14071–4.
[21] Wang X, Xiao C, Liu H, Chen M, Hao J, Wu Y. A study on fabrication of PVDF–HFP/PTFE blend membranes with controllable and bicontinuous structure for highly effective water-in-oil emulsion separation. RSC Adv 2018;8(49):27754–62.
[22] Chen L, Si Y, Zhu H, Jiang T, Guo Z. A study on the fabrication of porous PVDF membranes by *in-situ* elimination and their applications in separating oil/water mixtures and nano-emulsions. J Membr Sci 2016;520:760–8.
[23] Wang X, Xiao C, Liu H, Huang Q, Hao J, Fu H. Poly(vinylidene fluoride–hexafluoropropylene) porous membrane with controllable structure and applications in efficient oil/water separation. Materials 2018;11(3):443.

[24] Chen R, Xu J, Li S, Li Q, Wu H, He Q, et al. Multiscale-structured superhydrophobic/superoleophilic SiO_2 composite poly(ether sulfone) membranes with high efficiency and flux for water-in-oil emulsions separation under harsh conditions. New J Chem 2020;44(10):3824–7.
[25] Lei T, Lu D, Xu Z, Xu W, Liu J, Deng X, et al. 2D → 3D conversion of superwetting mesh: a simple but powerful strategy for effective and efficient oil/water separation. Sep Purif Technol 2020;242:116244.
[26] Ji D, Xiao C, An S, Liu H, Chen K, Hao J, et al. Preparation of PSF/FEP mixed matrix membrane with super hydrophobic surface for efficient water-in-oil emulsion separation. RSC Adv 2018;8(18):10097–106.
[27] Gao N, Xu ZK. Ceramic membranes with mussel-inspired and nanostructured coatings for water-in-oil emulsions separation. Sep Purif Technol 2019;212:737–46.
[28] Gu J, Xiao P, Chen J, Liu F, Huang Y, Li G, et al. Robust preparation of superhydrophobic polymer/carbon nanotube hybrid membranes for highly effective removal of oils and separation of water-in-oil emulsions. J Mater Chem A 2014;2(37):15268–72.
[29] Wu J, Li H, Lai X, Chen Z, Zeng X. Superhydrophobic polydimethylsiloxane@multiwalled carbon nanotubes membrane for effective water-in-oil emulsions separation and quick deicing. Ind Eng Chem Res 2019;58(20):8791–9.
[30] Yang J, Li HN, Chen ZX, He A, Zhong QZ, Xu ZK. Janus membranes with controllable asymmetric configurations for highly efficient separation of oil-in-water emulsions. J Mater Chem A 2019;7(13):7907–17.
[31] An YP, Yang J, Yang HC, Wu MB, Xu ZK. Janus membranes with charged carbon nanotube coatings for deemulsification and separation of oil-in-water emulsions. ACS Appl Mater Interfaces 2018;10(11):9832–40.
[32] Shi Z, Zhang W, Zhang F, Liu X, Wang D, Jin J, et al. Ultrafast separation of emulsified oil/water mixtures by ultrathin free-standing single-walled carbon nanotube network films. Adv Mater 2013;25(17):2422–7.
[33] Sun T, Feng L, Gao X, Jiang L. Bioinspired surfaces with special wettability. Acc Chem Res 2005;38(8):644–52.
[34] Pan J, Xiao C, Huang Q, Liu H, Zhang T. ECTFE hybrid porous membrane with hierarchical micro/nano-structural surface for efficient oil/water separation. J Membr Sci 2017;524:623–30.
[35] Yuan X, Li W, Zhu Z, Han N, Zhang X. Thermo-responsive PVDF/PSMA composite membranes with micro/nanoscale hierarchical structures for oil/water emulsion separation. Colloids Surf A 2017;516:305–16.
[36] Wei Y, Xie Z, Qi H. Superhydrophobic–superoleophilic SiC membranes with micro-nano hierarchical structures for high-efficient water-in-oil emulsion separation. J Membr Sci 2020;601:117842.
[37] Gu J, Fan H, Li C, Caro J, Meng H. Robust superhydrophobic/superoleophilic wrinkled microspherical MOF@rGO composites for efficient oil–water separation. Angew Chem Int Ed Engl 2019;58(16):5297–301.
[38] Mao H, Li SH, Zhang AS, Xu LH, Lu JJ, Zhao ZP. Novel MOF-capped halloysite nanotubes/PDMS mixed matrix membranes for enhanced *n*-butanol permselective pervaporation. J Membr Sci 2020;595:117543.
[39] Zhang WD, Sun W, Yang J, Ren ZQ. The study on pervaporation behaviors of dilute organic solution through PDMS/PTFE composite membrane. Appl Biochem Biotechnol 2010;160(1):156–67.
[40] Zhang N, Wu H, Li F, Dong S, Yang L, Ren Y, et al. Heterostructured filler in mixed matrix membranes to coordinate physical and chemical selectivities for enhanced CO_2 separation. J Membr Sci 2018;567:272–80.
[41] Zhu Y, Wang J, Zhang F, Gao S, Wang A, Fang W, et al. Zwitterionic nanohydrogel grafted PVDF membranes with comprehensive antifouling property and superior cycle stability for oil-in-water emulsion separation. Adv Funct Mater 2018;28(40):1804121.
[42] Zhang WH, Yin MJ, Zhao Q, Jin CG, Wang N, Ji S, et al. Graphene oxide membranes with stable porous structure for ultrafast water transport. Nat Nanotechnol 2021;16(3):337–43.